

Decomposition of Yttrium-Doped Barium Cerate in Carbon Dioxide

Robert D. Carneim, Theodore M. Besmann, Timothy R. Armstrong

Metals and Ceramics Division, Oak Ridge National Laboratory,
Oak Ridge, TN 37831 USA

Doped barium cerate and related perovskite ceramics currently dominate the high-temperature proton conductor field. Unfortunately, these materials have very stringent environmental limitations necessitating the costly and complex conditioning or cleaning of the application feed-gas. This work shows through both experimental results and thermodynamic modeling that $\text{Ba}(\text{Ce},\text{Y})\text{O}_{3-\delta}$ is ill-suited for use in environments containing CO_2 . Despite efforts to improve the stability of $\text{Ba}(\text{Ce},\text{Y})\text{O}_{3-\delta}$ through partial Zr_{Ce} substitution and adjusting the A-site to B-site cation ratio, the perovskite phase is shown to be unstable in the presence of CO_2 at temperatures below ca. 1000 °C.

Introduction

Proton conducting ion transport membranes are required to extract absolutely pure hydrogen from mixed gas streams in the processing of fossil fuels and other petroleum and petrochemical processes. Ceramic materials are required to withstand these high-temperature processes. Yttrium-doped barium cerate ($\text{BaCe}_{0.80}\text{Y}_{0.20}\text{O}_{3-\delta}$) is currently one of the best materials when considering only proton conductivity. However, this material is very sensitive to the carbon diox-

ide (CO_2) and sulfur (e.g., H_2S) contamination found in the fossil fuel process stream. Barium cerate will decompose into barium carbonate (BaCO_3) and ceria (CeO_2) in the presence of CO_2 ; and CeO_2 reacts with H_2S to produce a sulfided phase, particularly in the highly reducing fuel environment. Two approaches for improving the stability of barium cerate are examined: manipulation of the A- to B-site (in this case, Ba and Ce/Y/Zr, respectively) stoichiometry and partial substitution of Ce with Zr. Individually these techniques have been previously shown to enhance stability.^(1–4) In the present work, the effect of applying both modifications simultaneously is explored. High-temperature x-ray diffraction (HTXRD) and simultaneous thermogravimetric and differential thermal analysis (TGA/DTA) were used to determine decomposition temperatures, extent of decomposition, and reaction kinetics of various yttrium-doped barium cerate compositions in CO_2 -contaminated environments.

Experimental Procedure

Sample Preparation

Small batches (≈ 10 g) of powders were prepared by the glycine-nitrate process (GNP).⁽⁵⁾ Appropriate amounts of metal salts (barium-, cerium-, yttrium-, and zirconyl nitrates, ammonium cerium[IV] nitrate, and barium acetate were used as necessary [Alfa Aesar, Ward Hill, MA]) and glycine were dissolved in deionized water. The solution was heated on a hot-plate in a stainless steel beaker until a sufficient amount of solvent had evaporated allowing the precursor to ignite. The resulting ash was sieved (100-mesh) and calcined for 20 min to 30 min at 1200 °C to produce the desired single-phase perovskite. Additional material was obtained commercially (Praxair). The following compositions were synthesized:

- BCY—: Four compositions with varying barium stoichiometry: $\text{Ba}_x\text{Ce}_{0.80}\text{Y}_{0.20}\text{O}_{3-\delta}$ with $x = 1.00, 0.98, 0.95,$ and 0.90 ; designated BCY108, BCY88, BCY58, and BCY08, respectively.
- BCZ—: Three barium-deficient, non-acceptor-doped zirconium-substituted compositions: $\text{Ba}_{0.98}\text{Ce}_{1-y}\text{Zr}_y\text{O}_{3-\delta}$ with $y = 0.15, 0.10,$ and 0.05 ; designated BCZ885, BCZ89, and BCZ895, respectively.
- BCZY15: One barium-deficient, acceptor-doped, zirconium-substituted composition: $\text{Ba}_{0.98}\text{Ce}_{0.65}\text{Zr}_{0.15}\text{Y}_{0.20}\text{O}_{3-\delta}$; designated BCZY15.

The following compositions were purchased:

BCY—p: Two compositions with varying barium stoichiometry:
 $\text{Ba}_x\text{Ce}_{0.80}\text{Y}_{0.20}\text{O}_{3-\delta}$ with $x = 1.00$ and 0.98 ; designated BCY108p
and BCY88p, respectively.

High-Temperature X-Ray Diffraction

Initial phase identification of the calcined powders was carried out using room temperature powder x-ray diffraction (XRD) using Ni-filtered $\text{Cu } K\alpha$ x rays (Scintag PAD V diffractometer). High-temperature x-ray diffraction (HTXRD) was conducted with the same radiation in a Phillips X'Pert diffractometer with a platinum heater strip/sample stage in a hermetically sealed chamber (HTK 16 High-Temperature Camera). Resistance to degradation due to the presence of CO_2 was quantified by determining the temperatures at which BaCO_3 formed during heating and cooling of the single-phase perovskite in flowing CO_2 ($p_{\text{CO}_2} = p = 101 \text{ kPa}$ [1 atm]) using the following procedure (figure 1):

HTXRD: Heat sample in N_2 to $t = 1400 \text{ }^\circ\text{C}$ and cool to $200 \text{ }^\circ\text{C}$; perform scan; change sample environment to flowing CO_2 and hold 20 min ; perform scan; raise temperature by $50 \text{ }^\circ\text{C}$ and hold 5 min ; perform scan; repeat preceding two steps until $t = 1400 \text{ }^\circ\text{C}$; lower temperature by $100 \text{ }^\circ\text{C}$ and hold 10 min ; perform scan; repeat preceding two steps until $t = 500 \text{ }^\circ\text{C}$.

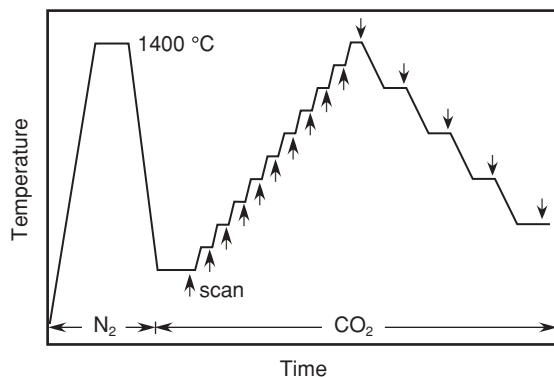


Figure 1. Schematic of temperature profile and gas flow schedule used for the high-temperature x-ray diffraction procedure.

Measurements were taken over the range from $2\theta = 20^\circ$ to $2\theta = 44^\circ$. Temperature was measured and controlled based on a type-S thermocouple welded to the bottom of the platinum strip. At sufficiently high temperatures ($t > 800^\circ\text{C}$), more accurate sample temperature measurements were possible through the use of an optical pyrometer (Optical Pyrometer, Leeds & Northrup Co., Philadelphia, PA) trained on the sample surface through a quartz window in the sample chamber.

Data obtained by the HTXRD procedure is presented by plotting the logarithms of the peak ratios (areas under peaks attributable to only the perovskite phase vs. those attributable to only non-perovskite phases; background intensity and noise ensure finite results), $\lg(r_{p/c})$, versus temperature during heating and cooling (figure 2). Based on examination of the raw XRD data, a cut-off value of $\lg(r_{p/c}) = -0.25$ was chosen to define transition temperatures— $\lg(r_{p/c}) > 0$ indicates no x-ray observable BaCO_3 and $\lg(r_{p/c}) < -0.5$ indicates the presence of a significant amount of BaCO_3 . The temperatures at which carbonate phase forms and disappears on heating, and forms again on cooling can be easily seen and compared.

An additional feature that stands out in this representation of the data is hysteresis in the high-temperature transition (i.e., the temperature at which BaCO_3 disappears on heating or appears on cooling). The high-temperature transition hysteresis, Δt_{hyst} , is defined as the difference between the transition temperatures measured during heating and cooling. This quantity may be used for comparing

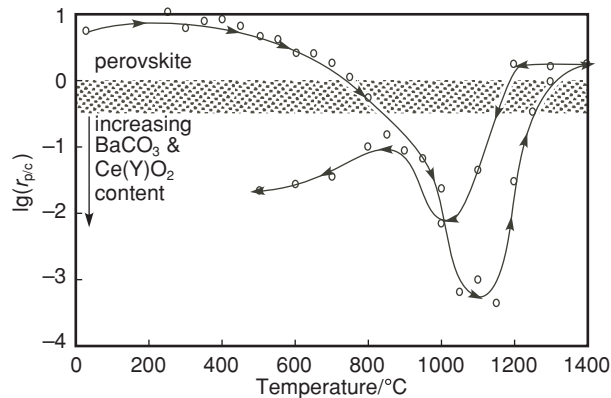


Figure 2. Example data set obtained by HTXRD showing raw data points from the individual scans, a freehand curve fit of the data (arrows indicate increasing time), and phase fields: top section indicates no detected decomposition products, the shaded section indicates just detectable BaCO_3 and Ce(Y)O_2 peaks, and the bottom region indicates significant decomposition.

reaction kinetics between related materials undergoing the same reaction at comparable temperatures.

Thermal Analysis

Simultaneous thermogravimetric analysis and differential thermal analysis (TGA and DTA) were performed (T/A Instruments SDT 2960 or Stanton Redcroft STA780) on select compositions. Multiple scans were performed on certain composition at heating rates between $\phi = 1.6 \text{ }^\circ\text{C}\cdot\text{min}^{-1}$ and $\phi = 25 \text{ }^\circ\text{C}\cdot\text{min}^{-1}$ in flowing CO_2 to allow estimation of the reaction activation energies using the Kissinger method.(6, 7) Additional experiments were carried out at $\phi = 1.6 \text{ }^\circ\text{C}\cdot\text{min}^{-1}$ in mixtures of flowing CO_2 and Ar-4% H_2 to examine the effect of CO_2 in reducing environments. The two overall gas compositions used were 3.85 % CO_2 + 3.85 % H_2 + 92.3 % Ar and 95 % CO_2 + 0.2 % H_2 + 4.8 % Ar (Air Liquide, Oak Ridge, TN).

Modeling

A thermodynamic equilibrium analysis was carried out to predict the transformation temperatures for reaction of BaCO_3 , CeO_2 , and $\text{YO}_{1.5}$ to $\text{BaCe}_{0.8}\text{Y}_{0.2}\text{O}_{3-\delta}$. Thermodynamic values (298 K heats for formation, 298 K entropies, and heat capacities) were obtained from the SGTE database (8) and calculations using FactSage™ computational thermodynamics software. Neither the SGTE database nor the literature contained values for the $\text{BaCe}_{1-z}\text{Y}_z\text{O}_{3-\delta}$, thus this phase was treated as an ideal solution of BaCeO_3 and $\text{BaYO}_{2.5}$. An ideal solution of the phases is a reasonable assumption given that BaCeO_3 and $\text{BaCe}_{0.8}\text{Y}_{0.2}\text{O}_{3-\delta}$ are both orthorhombic ($\text{BaYO}_{2.5}$ is not a reported phase). Data for these phases were obtained from the literature and estimates. The 298 K heat of formation and entropy of BaCeO_3 are $-1690 \text{ kJ}\cdot\text{mol}^{-1}$ and $144.5 \text{ J}\cdot\text{mol}^{-1}\cdot\text{K}^{-1}$, respectively.(9) The heat capacity of BaCeO_3 over the temperature range of interest was taken as the sum of the BaO and CeO_2 heat capacities provided by the SGTE database.

The 298 K heat of formation and entropy of $\text{BaYO}_{2.5}$ were estimated by interpolation of the values for the phases formed from the unary oxides along the $\text{BaO}\text{--}\text{YO}_{1.5}$ join; these were $-16 \text{ kJ}\cdot\text{mol}^{-1}$ and $2 \text{ J}\cdot\text{mol}^{-1}\cdot\text{K}^{-1}$, respectively.(10) These, together with the 298 K values for the unary oxides from the SGTE database, yielded the required 298 K enthalpy of formation and entropy: $-1524.5 \text{ kJ}\cdot\text{mol}^{-1}$ and $122.82 \text{ J}\cdot\text{mol}^{-1}\cdot\text{K}^{-1}$, respectively. Again, the heat capacity relations were found by summing the unary oxide values.

The phases CeO_2 and $\text{YO}_{1.5}$ are cubic and form extensive solid solutions, although with a significant miscibility gap.⁽¹¹⁾ For the purpose of the current calculations this was treated as a single ideal solid solution.

Results and Discussion

Barium Stoichiometry

HTXRD

Preliminary HTXRD experiments in CO_2 showed no differences in the behaviors of the three barium-deficient compositions (BCY88, BCY58 & BCY08), with BaCO_3 diffraction peaks becoming apparent at $t \leq 1050$ °C on cooling. This was deemed a slight improvement over the stoichiometric composition, BCY108, which presented BaCO_3 peaks already at $t \approx 1100$ °C on cooling. Initial results during heating showed no difference between the four compositions. Based on these preliminary results, any of the barium-deficient compositions would serve to realize improvement over the stoichiometric composition and stay well clear of a barium-excess situation which would result in severe degradation of electrical properties.^(1, 2) Therefore, the least (non-zero) barium-deficient composition ($x = 0.98$) was chosen for more detailed study.

Measurements performed on BCY108 and BCY88 using the HTXRD procedure described above revealed details of the differences in behavior of the stoichiometric and barium-deficient compositions with respect to degradation in CO_2 . The various transition temperatures are nearly identical for these two compositions (figure 3, Table I). The consequential difference between these two compositions is the extent of transformation: the peak ratio, $r_{p/c}$, is nearly one order of magnitude larger for BCY88 than for BCY108. The temperature range in which BaCO_3 is present and the high-temperature transition hysteresis were similar for these two compositions.

Thermal Analysis

The transition temperatures of these compositions as determined by DTA are consistently lower than as determined by HTXRD (Table I). There is good agreement in the DTA data between the synthesized and purchased powders (BCY88 and BCY88p, respectively), allowing comparisons between results of the two methods applied to different source powders. The DTA results, relative to the HTXRD results, are approximately 250 °C to 300 °C lower for the initial decom-

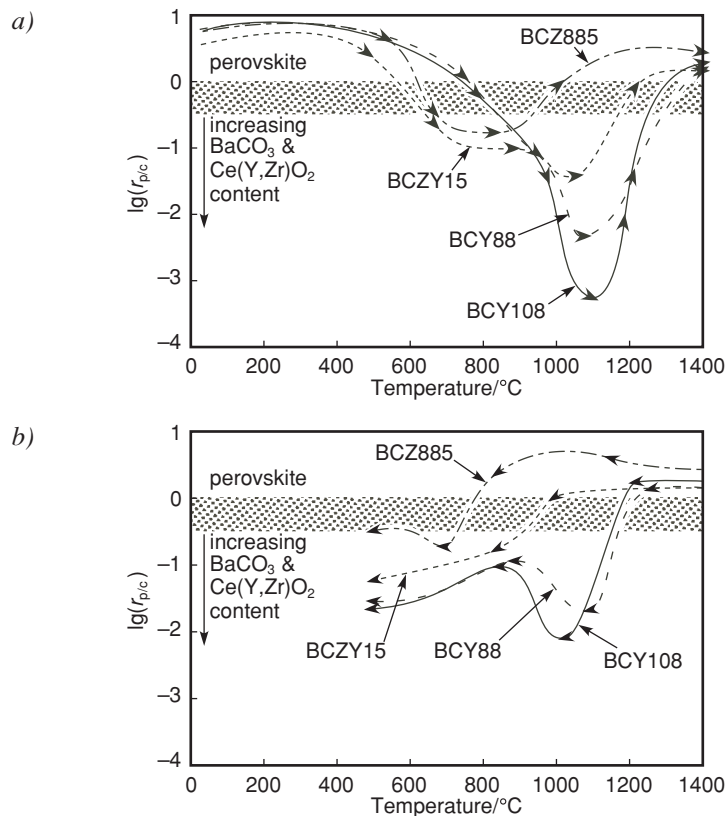


Figure 3. High-temperature x-ray diffraction results for $\text{BaCe}_{0.8}\text{Y}_{0.2}\text{O}_{3-\delta}$,
 $\text{Ba}_{0.98}\text{Ce}_{0.8}\text{Y}_{0.2}\text{O}_{3-\delta}$, $\text{Ba}_{0.98}\text{Ce}_{0.85}\text{Zr}_{0.15}\text{O}_{3-\delta}$,
and $\text{Ba}_{0.98}\text{Ce}_{0.65}\text{Zr}_{0.15}\text{Y}_{0.20}\text{O}_{3-\delta}$ during
heating (a) and cooling (b).

position on heating and approximately 50 °C to 150 °C lower for the subsequent reactions (perovskite formation on heating and decomposition on cooling).

The differences between the results obtained from the two methods arise due to a number of factors. The thermodynamic modeling results elucidate two features relevant at this point (figure 4a): $\text{BaCO}_3 + \text{Ce}(\text{Y})\text{O}_2$ is the stable low-temperature phase compositions; and secondly, there is a three-phase region in which the perovskite and the two decomposition products are in equilibrium approximately 155 °C wide. Therefore, at low temperature in CO_2 , the perovskite is metastable and the decomposition reaction is determined by kinetics. Slight differences in the sample configuration and experimental conditions can greatly

Table I. Summary of Results in CO₂ from HTXRD^a and DTA^b Experiments

Composition	Method	Decomp.	Perovskite	Decomposed	Decomp.	Hysteresis	Max. lg($r_{p/c}$)
		on Heating/ °C	forms on Heating/ °C	Temperature Range/ °C	on Cooling/ °C		Decomp. Peak Deflection ^c
BCY108	HTXRD	780	1280	500	1160	120	-3.25
BCY108p	DTA	486	1234	748	1056	178	n/a
BCY88	HTXRD	780	1330	550	1180	150	-2.35
BCY88	DTA	515 ^d	≈ 1188 ^e	≈ 673	1038	≈ 150	n/a
BCY88p	DTA	513	1239	726	1060	179	n/a
BCZ885	HTXRD	640	980	340	750	230	-0.80
BCZ885	DTA	550	1113	563	no rxn	n/a	n/a
BCZY15	HTXRD	600	1200	600	950	250	-1.45
BCZY15	DTA	539	1192	653	855	337	n/a

^a Tabulated values were extracted from data as in figure 2 using

lg($r_{p/c}$) = -0.25 cutoff value.

^b 4 °C·min⁻¹

^c N.B., lg($r_{p/c}$) < -0.5 ≡ significant decomposition.

^d Thermal analysis of the synthesized BCY88 powder shows a broad two-stage peak for this reaction; the reported value corresponds to the initial, but smaller peak.

^e Thermal analysis of this material showed a doublet peak; the average temperature is reported.

affect the observed transition temperature. Furthermore, the two methods detect different phenomena that are not necessarily dependent: the thermal analysis peaks reflect the addition of mass and the chemical reactions to incorporate that mass into the structure; this may all occur without immediately producing a crystalline phase, which is required for detection using the HTXRD method. Finally, the differences observed in the high-temperature reaction can further be due to the two methods being sensitive to the reaction at different points while traversing the three-phase region—HTXRD requires a certain amount of crystalline material to be present before it can be detected, while the DTA peak maximum corresponds to the maximum reaction rate; these two events do not necessarily occur simultaneously.

Environment

Table II summarizes the results obtained by DTA experiments and thermodynamic modeling for BCY108 in different atmospheres. Experiments in the 100 % CO₂ and 95 % CO₂ + 0.2 % H₂ (balance Ar) environments resulted in essentially identical transition temperatures. Reducing the CO₂ concentration to 3.85 % and

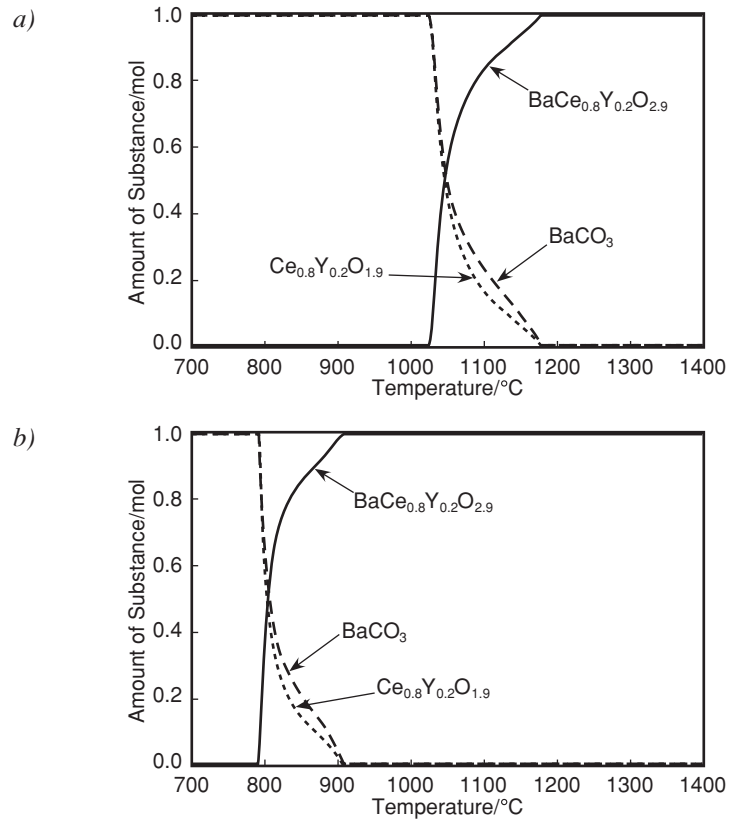


Figure 4. Thermodynamic modeling results for BaCe_{0.8}Y_{0.2}O_{3-δ} in CO₂ and 95 % CO₂ + 5 % 96Ar4H₂ (calculation for these two environments produced indistinguishable plots) (a) and in 3.85 % CO₂ + 96.15 % 96Ar4H₂ (b).

Table II. Summary of DTA^a and Modeling Results of BaCe_{0.8}Y_{0.2}O_{3-δ} in Different Gas Mixtures

Gas Composition	Decomposition on Heating/°C	Perovskite Formation on Heating/°C	Decomposition on Cooling/°C	Equilibrium 3-Phase Field Range/°C
CO ₂	470	1225	1062	1025–1180
95CO ₂ +0.2H ₂ +4.8Ar	477	1206	1054	1025–1180
3.85CO ₂ +3.85H ₂ +92.3Ar	510	945	717	795–910

^a 1.6 °C·min⁻¹

including an equal amount of H₂ (balance Ar) resulted in a slightly higher transition temperature for the low-temperature reaction and significantly lower transition temperatures (i.e., during both heating and cooling) for the high-temperature reaction.

The temperature at which the metastable perovskite decomposes (i.e., the low-temperature reaction during heating) increased a mere 7 °C when the CO₂ concentration was reduced from 100 % to 95 %. Further reduction in CO₂ concentration to 3.85 % resulted in a further reaction temperature increase of only 33 °C. The high-temperature reaction was also not significantly affected by the reduction in CO₂ concentration from 100 % to 95 % and addition of 0.2 % H₂. There was a significant response to the further reduction in CO₂ concentration to 3.85 % and relative increase in H₂-content (H₂:CO₂ increased from 1:475 to 1:1). The reaction temperature decreased by approximately 300 °C.

Modeling

Equilibrium calculations were performed over the temperature range 700 °C to 1400 °C for the initial composition 1 mol BaO, 0.8 mol CeO₂, and 0.2 mol YO_{1.5}. The above solution phases and all known condensed phases were included in the calculations at 1 bar total pressure and the three different gas compositions. The only stable phases computed to be present under all conditions were BaCO₃ and the two solution phases (figure 4). The results for 100 % CO₂ and the high CO₂:H₂ ratio were identical (figure 4a). From 700 °C to 1025 °C the Ce_{0.8}Y_{0.2}O_{1.9} solution phase was the only stable condensed phase. Between 1025 °C and 1180 °C there is a continuous conversion of the Ce_{0.8}Y_{0.2}O_{1.9} phase to the perovskite phase with concomitant compositional changes within the phases (i.e., the Ce:Y ratio is not constant in each phase within the transformation temperature range). Above 1180 °C only the BaCe_{0.8}Y_{0.2}O_{2.9} is stable. At the lower CO₂:H₂ ratio the reaction forming the perovskite occurs at lower temperatures (figure 4b). The DTA results are in amazingly good agreement with the predicted phase diagrams produced by this relatively simple ideal solution model. The ranges defined by the hysteresis in the DTA data correlate closely with the ranges defined by the predicted 3-phase fields in the model (Table II).

Zirconium Substitution

Undoped

Preliminary HTXRD results in CO₂ on the three Ba_{0.98}Ce_{1-y}Zr_yO_{3-δ} compositions showed BaCO₃ formation in the two lower Zr-content samples (y = 0.05 and

0.10) and no x-ray detectable decomposition products in the $y = 0.15$ sample (BCZ885). The two lower Zr-content compositions were abandoned and the detailed HTXRD analysis and DTA were performed on BCZ885. This composition had considerably improved chemical stability over the most similar non-zirconium-substituted composition, the acceptor-doped composition BCY88. The data just enters the BaCO_3 region of the $\lg(r_{p/c})$ vs. t plot during both heating and cooling (figures 3a and 3b, respectively), and the DTA/TGA experiments showed no decomposition on cooling whatever (Table I). Furthermore, the temperature range in which BaCO_3 is present is smaller ($t_{\text{range}} \approx 340$ °C vs. 550 °C) and occurs at lower temperatures.

Yttrium-Doped

Zirconium substitution resulted in significantly improved chemical stability in CO_2 ; however, the material must be acceptor doped to provide any hope of practical proton conductivity. The composition BCZY15 incorporates the stability-enhancing modifications examined earlier—slight Ba deficiency and 0.15 Zr_{Ce} substitution—and reintroduces the standard 0.20 Y doping. The HTXRD analysis and DTA in CO_2 show that BCZY15 exhibits an intermediate behavior. On heating, BCZY15 possesses characteristics of both the two simpler compositions (i.e., BCY88 and BCZ885): a minor excursion into BaCO_3 territory at $t \approx 600$ °C, similar to BCZ885; then further BaCO_3 formation above $t \approx 1000$ °C, approximately the temperature of maximum conversion to BaCO_3 of BCY88. The extent of conversion is also intermediate to the two simple compositions. On cooling, BCZY15 behaves slightly differently. Barium carbonate begins to form at a temperature approximately midway between the onset temperatures for BCY88 and BCZ885. But rather than distinct peaks in the $\lg(r_{p/c})$ data—as BCY88 has at $t \approx 1050$ °C and BCZ885 at $t \approx 700$ °C—BCZY15 displays a gradual, monotonic decrease in $\lg(r_{p/c})$.

Since BCZY15 behaves approximately as a combination of the two component compositions, the magnitudes of the BaCO_3 -presence temperature range and high-temperature transition hysteresis are approximately equal to the greater of the two corresponding values for the simple compositions: $t_{\text{range}} \approx 600$ °C, comparable to the t_{range} value for BCY88; and $\Delta t_{\text{hyst}} \approx 250$ °C, similar to the Δt_{hyst} value of BCZ885. Furthermore, the high-temperature transition temperatures of BCZY15 fall between those of BCY88 and BCZ885 while the hysteresis is still comparable to that of BCZ885.

Kinetics

Two methods of characterizing the reaction kinetics were employed. The hysteresis in the high-temperature reaction temperature (Δt_{hyst} ; i.e., the difference between the transition temperatures observed during heating and cooling) provides a qualitative measure of reaction kinetics for similar materials at comparable temperatures. And the change in the reaction temperatures during heating as a function of heating rate allows the calculation of the reaction activation energies for both the low-temperature decomposition reaction of the metastable phase as well as the high-temperature reaction. Figure 5a illustrates this effect for the high-temperature transition in BCY108p, with the corresponding Kissinger analysis plot in figure 5b.

Considering first the compositions BCY88 and BCZ885, it is clear that the high-temperature transition occurs at significantly lower temperatures in BCZ885. The high-temperature transition hysteresis, however, is greater: $\Delta t_{\text{hyst}} \approx 230$ °C for BCZ885 (when this reaction occurs) vs. $\Delta t_{\text{hyst}} \approx 150$ °C to 179 °C for BCY88. Such an increase in this quantity indicates an increase in the energy barrier for this reaction. This is supported by the calculated activation energies (Table III). The activation energy for this reaction in BCZ885 is approximately three times its activation energy in BCY88. (The difference in the activation energies calculated for the synthesized and purchased powders—BCY88 and BCY88p, respectively—is likely due to differences in powder characteristics such as surface area and amorphous content.)

The high-temperature transition temperatures of BCZY15 fall between those of BCY88 and BCZ885 while the hysteresis is still comparable to that of BCZ885. However, the calculated activation energy—though it does fall between the values for BCY88 and BCZ885—is comparable again to that for BCY88. This discrepancy indicates that the materials being compared are too dissimilar to allow estimation of the relative kinetics using the temperature hysteresis.

The calculated activation energies for the initial decomposition of the perovskite on heating were not influenced greatly by the compositional changes studied in this work. For this reaction, the highest value obtained for these materials was only approximately 1.6 times the lowest value (cf. the factor of 3 difference for the high-temperature reaction). Furthermore, the observed activation energies for the initial composition is relatively low due to the elevated internal energy inherent in metastable phases.

Summary and Conclusion

Two methods for improving the stability of yttrium-doped barium cerate in CO₂ have been investigated. Producing slightly barium-deficient compositions

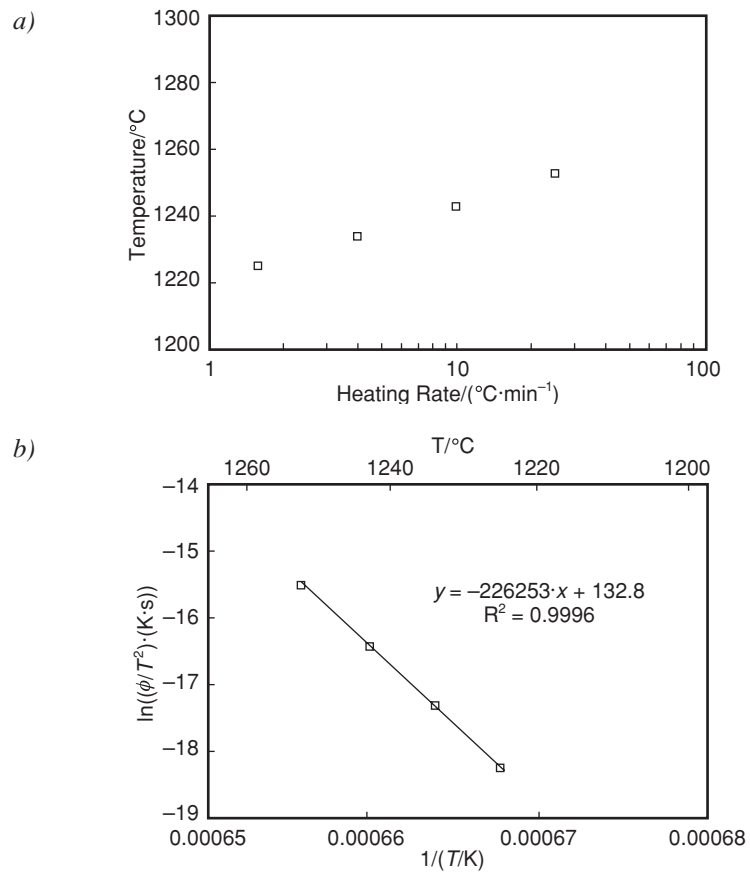


Figure 5. Example data set used for calculation of reaction activation energies (BCY108p, perovskite formation on heating): change in DTA peak temperature with changing heating rate (a) and the same data plotted in the form of the Kissinger equation (b)—the slope of this line is $-E/R$, where E is the activation energy and R is the universal gas constant.

and partial substitution of Zr for Ce have been previously and in this work shown to increase the resistance to decomposition in the presence of CO₂. The effects of the individual modifications as well as their combined effects have been shown utilizing thermal analysis and high-temperature x-ray diffraction. While definite improvements in CO₂-tolerance were observed, absolute immunity was not achieved at the levels of modification studied. Since it is known (8, 9) that significant amounts of Zr_{Ce} substitution or Ba-deficiency severely decrease conductivity,

Table III. Reaction Activation Energies^a in CO₂ on Heating

<i>Composition</i>	<i>Decomposition on Heating/(kJ·mol⁻¹)</i>	<i>Perovskite Formation on Heating/(kJ·mol⁻¹)</i>
BCY108p	242	1881
BCY88p	205	2142
BCY88	148 ^b	1452 ^c
BCZ885	163	4152
BCZY15	230	1735

^a Calculated by the Kissinger equation using results from up to four heating rates. ($R^2 > 0.95$)

^b Initial, but smaller peak used.

^c Average temperature of doublet peak used.

the prospect of producing a practical, durable high-temperature proton conductor in this system with these techniques is unlikely.

Acknowledgment

This project was sponsored by the Office of Fossil Energy. The Oak Ridge National Laboratory is operated by UT-Battelle, LLC for the U.S. Department of Energy under Contract DE-AC05-00OR22725.

References

1. Shima, D.; Haile, S. M. *Solid State Ionics*, **1997**, *97*, 443–55.
2. Ma, G.; Shimura, T.; Iwahara, H. *Solid State Ionics*, **1998**, *110*, 103–10.
3. Ryu, K. H.; Haile, S. M. *Solid State Ionics*, **1999**, *125*, 355–67.
4. Taniguchi, N.; Nishimura, C.; Kato, J. *Solid State Ionics*, **2001**, *145*, 349–55.
5. Chick, L. A.; Pederson, L. R.; Maupin G. D.; Bates, J. L.; Thomas, L. E.; Exarhos, G. J. *Mater. Lett.*, **1990**, *44* (1, 2), 6–12.
6. Kissinger, H. E. *J. Res. Natl. Bur. Stand.* **1956**, *57* (4), 217–21.
7. Kissinger, H. E. *Anal. Chem.* **1957**, *29* (11), 1702–6.
8. *SGTE Pure Substance Database*, 1996 Version, Scientific Group Thermodata Europe.
9. Cordfunke, E. H. P.; Booji, A. S.; Huntelaar, M. E. *J. Chem. Thermodyn.* **1998**, *30*, 437–47.
10. Kale, G. M.; Jacob, K. T. *Solid State Ionics* **1989**, *34*, 247–52.
11. Longo, V.; Podda, L.; *J. Mater. Sci.* **1981**, *16* (3), 839–41.